

# AERODYNAMICS OF A FINITE WING WITH SIMULATED ICE

510-02

160470

N 93-27437

M. B. Bragg\*, A. Khodadoust\*, and M. Kerho†

University of Illinois at Urbana-Champaign  
Urbana, Illinois

## ABSTRACT

The effect of a simulated glaze ice accretion on the aerodynamic performance of a three-dimensional wing is studied experimentally. Results are reviewed from earlier two-dimensional tests which show the character of the large leading-edge separation bubbles caused by the simulated ice accretion. The 2-D bubbles are found to closely resemble well known airfoil laminar separation bubbles. For the 3-D experiments a semispan wing of effective aspect ratio five was mounted from the sidewall of the UIUC subsonic wind tunnel. The model uses a NACA 0012 airfoil section on a rectangular planform with interchangeable tip and root sections to allow for 0- and 30-degree sweep. A three-component sidewall balance was used to measure lift, drag and pitching moment on the clean and iced model. Fluorescent oil flow visualization has been performed on the iced model and reveals extensive spanwise and vortical flow in the separation bubble aft of the upper surface horn. Sidewall interaction and spanwise nonuniformity are also seen on the unswept model. Comparisons to the computed flow fields are shown. Results are also shown for roughness effects on the straight wing. Sand grain roughness on the ice shape is seen to have a different effect than isolated 3-D roughness elements.

## I. INTRODUCTION

The operation of aircraft in icing conditions are affected by large performance penalties due to ice accretion on unprotected surfaces. Understanding the aerodynamic penalties due to ice accretion on both lifting and non-lifting surfaces is important since many components are not ice protected. The initial cost, cost of maintenance and weight penalty associated with ice protection systems makes their use practical on only the most critical components.

Most icing experiments, where aerodynamic measurements have been made, have only dealt with two-dimensional aircraft components. The experimental work of Bragg et. al.<sup>1-3</sup>, and the corresponding computational research of Potapczuk<sup>4</sup>, Cebeci<sup>5</sup>, and Sankar<sup>6</sup>, have focused on a 2-D NACA 0012 airfoil with a simulated glaze ice accretion. Only the most recent work, Bragg et. al.<sup>7-9</sup> and Kwon<sup>10</sup> have begun to investigate the flow field about a wing with simulated glaze-ice accretion. Bragg<sup>7</sup> measured the surface

pressures on a straight aspect ratio 5 wing with a NACA 0012 section and the simulated ice shape of ref. 1 - 3. Kwon<sup>10</sup> compared Navier-Stokes calculations to these data and showed good results except near the root where the sidewall boundary conditions differed. Sankar<sup>11</sup> modeled the tunnel sidewall and improved the prediction near the root. Khodadoust<sup>5</sup> and Bragg<sup>5</sup> extended the 3-D wing pressure measurements to include the effect of wing sweep.

In this paper, the 3-D results on both the straight and swept wing will be reviewed. Emphasis will be on the experimental results with some comparison to the computational data. Flow visualization results will be presented which clearly show the very 3-D features of the flow field about the iced, swept wing. The effect of sandgrain and isolated 3-D roughness on the unswept wing are discussed. The two roughness models are shown to have a very different effect on the wing maximum lift coefficient. However, first a brief review of earlier 2-D data taken using

\* Associate Professor, Department of Aeronautical and Astronautical Engineering, Associate Fellow AIAA.

† Graduate Research Assistant, Department of Aeronautical and Astronautical Engineering, Member AIAA.

this ice shape should help put the current 3-D results in perspective.

## II. EXPERIMENTAL PROCEDURE

The most recent tests were conducted in the subsonic wind tunnel at the University of Illinois at Urbana-Champaign. The tunnel is of conventional design with approximately a three-by-four foot test section, eight feet in length. The tunnel operates at speeds from zero to 165 mile per hour at Reynolds numbers of up to  $1.5 \times 10^5$  per foot. The tunnel is of open return type and uses four turbulence screens and honeycomb in the settling chamber to reduce tunnel turbulence to approximately .07 percent. Earlier experimental data were acquired in a similar, three-by-five foot tunnel, at The Ohio State University.

The 2-D model used for these tests was a 21-inch chord NACA 0012 airfoil. The first 15 percent of the leading edge was removable so a simulated ice accretion could be installed. The ice accretion used was a simulation of that measured on a NACA 0012 airfoil in the NASA Icing Research Tunnel, Fig. 1. The icing conditions were a free-stream velocity of 130 mph, angle of attack of 4 degrees, icing time of 5 minutes, volume median diameter droplet of 20 microns, LWC=2.1 g/m<sup>3</sup> and a temperature of 18° F. Under these conditions the ice which accretes is considered glaze. Data on the 2-D model was taken from its approximately 95 surface pressure taps and a wake-survey probe. Detailed measurements were taken in the separation bubble with a split hot-film probe<sup>3</sup> which could detect and measure reverse flow.

The 3-D model used for this test is a semispan wing with a chord of 15.0 inches and a span of 37.5 inches when in the unswept position, Fig. 2. The swept wing has a sweep of 30 degrees and a span of 35.18 inches. A NACA 0012 airfoil section was chosen to compare to earlier 2-D tests. The model consists of several components to allow wing sweep and to allow different simulated ice shapes to be tested through interchangeable leading edges. Two leading edges have been constructed for the model ahead of the 15 percent station, a NACA 0012 leading edge and the simulated glaze ice accretion.

The model is equipped with surface static pressure taps. The taps are located in 5 major rows plus a row on the tip section. The centerline

row of taps has 80 taps in the no-ice configuration and 83 in the iced configuration. The other 4 rows on the main element have 40 and 41 taps in the no-ice and iced configurations, respectively. Including the 21 taps on the wing tip section, the model has a total of 261 taps in the no-ice configuration and 268 taps in the iced configuration. Pressure measurements were made using 6 Scanivalves.

A three-component sidewall balance was designed and constructed for the 3-D experiment. The balance is used to determine model lift, drag and pitching moment by measuring the normal, axial and moment. The balance is mounted outside the tunnel with the model spar passing through the tunnel wall and down the center of the balance. A 0.1 inch gap was left between the model and the sidewall to avoid any balance interference. Doubling the gap had no measurable effect on the model measured loads. Balance calibration resulted in linear primary coefficients and balance interactions.

Flow visualization was performed on the models using fluorescent oil. The oil is placed on the models and the tunnel is run until the flow pattern is established. The oil is illuminated with ultraviolet light and photographed with a 35mm camera. The flow visualization was performed at a chord Reynolds number of 1.2 million.

Data acquisition and reduction was performed at UIUC using an AT&T 6386WGS PC and the ASYST version 3.1 software written by ASYST Technologies Software Inc. A Data Translation model DT2821-F16SE A to D board (12 bit, 16 channel and 140kHz) was used to acquire the data. The sensors were excited, and the outputs filtered and gained as needed by eight Measurement Group model 2200 signal conditioners.

The pressure data, both model surface pressures and facility transducers, were acquired and reduced in the usual fashion and a detailed discussion will not be presented here. Pressure data were taken at a nominal Reynolds number of 1.5 million. Model pressures were converted to pressure coefficients using the tunnel dynamic pressure measured on each of the Scanivalves. Note that when span loads are shown, Y is taken parallel to the leading edge and C<sub>l</sub> is taken along the tap lines perpendicular to the leading edge. Balance data were acquired using 300 samples per channel at 200 Hz and averaged to get one data point. The balance and model gravity tares are taken and subtracted from the data. Wall

corrections are made to the data based on the method of Rae and Pope<sup>12</sup>. These data were taken at a chord Reynolds number of 1.2 million.

### III. RESULTS AND DISCUSSION

#### 2-D Results

Two-dimensional experimental results on an airfoil with a simulated ice accretion have been taken by Bragg et. al.<sup>1-3</sup>. The results shown are with and without the simulated glaze ice accretion shown in Fig. 1. Glaze ice accretions are characterized by the "horns" which are the spoiler like protrusions that are formed. These horns cause significant alteration of the airfoil flow field through the formation of separation bubbles. Here some information on these bubbles is presented as an introduction for the 3-D data. A more detailed discussion of the 2-D ice-induced separation bubbles can be found in ref. 13.

Figure 3 shows the split hot-film measured velocity profiles in the upper and lower surface separation bubbles at an angle of attack of 4 degrees. First, consider the upper surface measurements. The first profile is taken at  $x/c = -0.02$ , just behind the ice horn. The flow is separated here with a very thin region of reverse and shear flow. The reverse flow region grows rapidly as we move downstream to  $x/c = 0.02$ . Note that the reverse flow is very slow, rarely exceeding 20 ft/sec or about 15 percent of the free-stream velocity. As the flow moves downstream the shear layer thickens and the amount of reverse flow decreases until the boundary layer reattaches around  $x/c = 0.16$ . Immediately downstream a distorted turbulent boundary layer is seen. Flow in the lower surface bubble is similar with reattachment of the bubble occurring between  $x/c = 0.12$  and  $0.14$ . Similar trends are also seen at 0 and 2 degrees angle of attack.

In Fig. 4 the measured pressure distribution about a NACA 0012 airfoil, with and without the simulated ice accretion of Fig. 1, is shown. The clean airfoil shows the well known pressure distribution about a NACA 0012 airfoil. Looking on the upper surface of the iced airfoil, a region of almost constant pressure is seen extending from the leading edge to  $x/c = 0.08$ . This indicates that a leading-edge separation bubble is present. These bubbles, although quite large, act like classical airfoil laminar separation bubbles<sup>13, 14</sup>. The bubble and shear layer are initially laminar with shear layer transition occurring in the region

where the constant pressure ends. The turbulent mixing in the shear layer leads to reattachment downstream after some degree of pressure recovery. In this case reattachment occurs at  $x/c = 0.16$ <sup>13</sup>. A separation bubble is also seen in the pressure distribution on the lower surface. Its behavior is similar to the upper surface bubble. Note that comparing the pressure distribution to the profiles of Fig. 3, the largest reverse flow velocity occurs at  $x/c = 0.08$ , the end of the constant pressure plateau. This compares qualitatively to the classic model of a reattachment vortex in a laminar separation bubble.

Figure 5 shows the bubble size and shape as indicated by the separation streamlines for the upper and lower surface bubbles calculated from the mean velocity measurements. At  $\alpha = 0$  degrees both upper and lower surface bubbles are quite large. As the angle of attack increases, the upper surface bubble grows slowly from 0 to 2 degrees and more rapidly from 2 to 4 degrees. Between 4 and 6 degrees the bubble grows rapidly and the bubble becomes unsteady. The bubble fails to reattach at angles much above 6 degrees. The lower surface bubble decreases rapidly in size at first as  $\alpha$  is increased, but changes little in length between 2 and 4 degrees angle of attack. The location of maximum bubble thickness measured normal to the surface occurs at the transition location for bubbles on smooth airfoils<sup>14</sup>. However, here due to the surface geometry, this does not correlate to the transition locations indicated by the surface pressures.

Measured boundary-layer momentum thickness for the upper surface taken from the split hot-film data<sup>13</sup> are shown in Fig. 6. The momentum thickness grows rapidly from the separation point at a rate relatively independent of angle of attack. For angles of attack of 0, 2 and 4 degrees a maximum value is reached in the bubble. This maximum value moves downstream with angle of attack,  $x/c = .02, .04$  and  $.08$  respectively, and the maximum value increases with angle of attack. A local minima is reached further downstream in the vicinity of, but slightly ahead of the reattachment point. The values are  $x/c = .06, .08$  and  $.14$ , for the angles of attack of 0, 2 and 4 degrees, respectively. Downstream of the bubble reattachment, the momentum thickness rises slightly, falls again, then grows steadily over the region  $x/c = 0.3$  to the trailing edge. At 6 degrees angle of attack the character of the curve has changed. Here reattachment is shown by a leveling off of the momentum thickness and a slight decrease around  $x/c = .35$ . The momentum thickness rises rapidly thereafter.

This simulated iced airfoil reaches maximum lift at 7 degrees angle of attack and the bubble is completely burst at 8 degrees angle of attack. At 6 degrees the separated flow is observed to be very unsteady and the bubble large and approaching a bursting condition.

Briley and McDonald<sup>15</sup> show calculated momentum thickness values in a laminar separation bubble on a NACA 66<sub>3</sub>-018 airfoil. Their results show a slight reduction in momentum thickness after shear layer transition, and a rapid rise occurring just before reattachment. These trends compare well to the data presented here. In fact, as shown in reference 13, the measurements made in the separation bubble aft of the ice horn compare qualitatively to a classic laminar separation bubble of the long bubble type.

### 3-D Results

A sketch of the 3D model in the swept and straight configurations is shown in Fig. 2. Initial tests with the 3-D model were carried out in the straight-wing configuration. These tests were conducted primarily to generate data to compare to the 2-D data already available<sup>1-3</sup>. More recent measurements, which have been used for comparison to the Navier-Stokes computations of Kwon and Sankar, have utilized the 3-D model in both the swept and straight configurations.

Figure 7 shows flow visualization results on the straight wing at  $\alpha = 4$  and  $8^\circ$ . At 4 degrees the oil flow reveals a very 2-D flow. The only 3-D character is a small interaction seen with the wing tip vortex. Although difficult to see in these reproductions, an ice-induced separation bubble exists at the leading edge. It reattaches around 15 percent chord. In the 8 degree case the bubble reattachment can be seen to vary greatly in the spanwise direction. The maximum extent of the bubble is over fifty percent chord, about 1/3 of the semispan inboard. Due to the 3-D induced flow, the effective angle of attack reduces as the wing tip is approached, and the bubble reattachment moves forward. Near the root, the bubble also reduces in length. This is due to a sidewall separation which forces early reattachment of the bubble<sup>11,16</sup>.

The presence of spanwise flow on the wing is greatly affected by the wing sweep. This result can be seen in CFD flow visualization<sup>17</sup> shown in Fig. 8. For the CFD flow visualization, the location of several massless air-stream particles is

tracked over the wing. The  $\alpha = 4^\circ$  flow visualization clearly shows the formation of a leading edge vortex. This vortex forms in the separation bubble aft of the upper surface ice horn. The vortex grows in diameter as it moves out from the root to the tip. Spanwise velocities in the vortex are seen to be quite large<sup>9</sup>. Also note that significant spanwise flow is seen aft of the leading-edge vortex, particularly near the tip.

The CFD particle-trace flow visualization shows a complex flow field for the iced swept wing at  $\alpha = 8^\circ$ . The leading edge separation bubble seen at 4 degrees has now enlarged significantly. The particles tracked in the separation bubble are shown to heavily interact with the particles tracked on the wing further downstream. This is partly due to the stall characteristics of a swept wing. A swept wing tends to stall at the wing tip first. The CFD flow visualization shows a massively separated flow region on the swept wing starting near the wing tip and extending into the midspan region of the wing, engulfing the separation bubble region.

In Fig. 9, experimental and computational surface flow visualization results are shown. The computational results are from simulated oil flow generated by tracing the trajectories of massless particles introduced into the Navier-Stokes flow field. The experiment was conducted at a chord Reynolds number of 1.2 million while the computation was carried out at 1.5 million. Here, the leading edge vortex grows in size as it moves from the root to the tip. In the computational result, the reattachment line moves back to about 80 percent chord near the tip. Ahead of this line the vortex-induced surface flow is forward into the free stream and towards the tip as before. A similar result is seen in the experimental data. Near the tip the flow is essentially parallel to the trailing edge behind the reattachment line. The interaction of the large leading-edge vortex and the tip vortex causes an interesting flow at the tip. The flow moves forward toward the leading edge then turns back towards the trailing edge, all the time flowing outboard. Near the trailing edge this motion is more pronounced in the experimental data. The experimental data shows a somewhat different flow at the tip in the midchord to leading-edge region. This is probably due to the simpler leading-edge geometry used in the CFD model.

Span loads for both the iced and no-iced configurations of the 3-D straight wing are shown in Fig. 10. These data were obtained by integrating the pressure data to obtain sectional lift coefficients. At 0 and 2 degrees angle of

attack the two span loads are amazingly similar. This indicates, as can also be seen in the 3-D lift, that the zero-lift angle and lift-curve slopes are not affected by the simulated ice. It is well known that a straight rectangular wing stalls first at the root. This is clearly seen in the iced span load data as the sectional lift values on the inboard wing fall below those of the clean model as the angle of attack is increased. This occurs due to the bursting of the ice-induced separation bubble near the root where the effective angle of attack is high.

The spanwise wing loading for the swept wing is shown in Fig. 11 for positive angles of attack from 0 to 8 degrees. As expected, the presence of the ice shape has caused a reduction in wing loading, especially on the outboard sections where stall occurs first on a swept wing. Contrast this to the straight wing in Fig. 10 where the root stalls first.

As a part of the experimental icing research, the effect of roughness was studied on the aerodynamic performance of the straight wing in the iced and un-iced configurations. Two types of roughness were examined on the straight wing: isotropic and three-dimensional roughness. The isotropic roughness was a 50-grit sandpaper roughness with  $k/c = 0.0010$ . The 3-D roughness were  $0.25 \times 0.25$  inch squares, 0.054 inch high, placed offset 0.5 inches apart in rows. In Fig. 12, the section lift performance of the smooth ice shape is compared with the section lift performance of the iced wing when isotropic and 3-D roughness is added. The results indicate that in the linear region,  $\alpha = -6$  to  $6$  deg., neither the isotropic nor the 3-D roughness significantly affect the lift performance of the wing. In the non-linear region, the isotropic roughness has little effect on the positive stall angle, with a small reduction in maximum lift. At negative angles of attack, an earlier stall onset is seen with a reduction in lift due to the roughness.

The effect of the 3-D roughness on the section performance of the model seems to be somewhat different in the stall regime. Here, a distinct stall angle can not be detected in either the positive or the negative range of angles of attack. Rather, at the angle where the wing section stalls in the smooth-ice case, the lift-curve slope changes but the lift continues to increase.

This phenomena could be attributed to the size of the three-dimensional roughness used. The 3-D roughness is three times larger than the particles which form the isotropic roughness. The

result of the particles' action is similar to the results of vortex generators. The effect of the roughness becomes particularly evident near the stall regime. In this regime, the flow seems to remain attached somewhat longer, therefore producing a potentially softer stall at both positive and negative angles of attack. Neither of these two types of roughness may correctly model the actual 3-D, and highly irregular roughness found on actual ice accretions. More research on surface roughness effects is needed.

The lift performance of the straight wing, measured with a three component balance, is shown in Fig. 13. Comparison between the clean wing, the clean wing with roughness, and the iced wing with rough leading edge reveal no appreciable change in the lift curve slope of the wing. The angle of stall, however, is shown to be directly affected by the presence of roughness. The straight wing stalls at  $\alpha = 17^\circ$  in the clean configuration. With the addition of roughness, the stall angle is reduced to  $13^\circ$ . The presence of leading edge ice in addition to roughness further reduces the stall angle to  $10^\circ$ . In addition to the stall angle, roughness is shown to affect the post stall performance of the straight wing.

#### IV. SUMMARY

The glaze ice accretion studied in this paper had a severe effect on the aerodynamics of the NACA 0012 airfoil. The 2-D data clearly showed the laminar separation bubble which is a dominant feature of the iced airfoil flow field. The bubble causes a large drag increase and early airfoil stall when the bubble bursts and fails to reattach. The bubble has the characteristics of a classic long bubble type airfoil laminar separation bubble. A straight aspect ratio five wing was tested with the same simulated ice accretion. Flow visualization results showed a fairly 2-D flow on this unswept wing. Significant sidewall boundary-layer interaction was seen in the flow visualization as well. The wall boundary layer in the tunnel affected the results by delaying the root stall. When this was modelled properly in the CFD code the results for span load compared favorably.

The swept wing was seen to have a very three-dimensional flow field. At low angle of attack, flow visualization shows a strong leading edge vortex formed in the separated flow aft of the upper surface ice horn. Spanwise flow in the vortex is significant. As the angle of attack is

increased, the vortex grows, especially near the tip, and a very three-dimensional flow develops. Since the swept wing stalls first at the tip, the wall boundary layer has little effect on these results. Comparison of the experimental results to the computations are good.

Surface roughness effects were presented on the unswept wing. Both sandgrain roughness and isolated 3-D roughness elements were placed on the simulated ice accretion. The effects were exactly the opposite with the 3-D roughness actually increasing the maximum lift of the iced, unswept wing. Much more research is needed on roughness effects on iced airfoils and its effect on the leading-edge separation which is so critical to the iced airfoil performance. Roughness models more complex than simple sandgrain roughness will have to be developed to properly reproduce actual ice roughness effects.

Future research will include laser Doppler velocimeter data for a more detailed look at these 3-D flow fields. This will provide a more complete picture of the 3-D separation bubbles. Research on roughness effects and its proper modelling are also underway to improve our understanding of this complex flow.

#### ACKNOWLEDGEMENT

This work was supported in part by a grant from NASA Lewis Research Center. The authors wish to thank Dr. M. G. Potapczuk of NASA Lewis for his support of this research.

#### REFERENCES

1. Bragg, M. B. and Coirier, W. J., "Aerodynamic Measurements of an Airfoil with Simulated Glaze Ice", AIAA-86-0484, paper presented at the 24th Aerospace Sciences Meeting, Reno, Nevada, Jan. 6-9, 1986.
2. Bragg, M. B. and Spring, S. A., "An Experimental Study of the Flow Field about an Airfoil with Simulated Glaze Ice", AIAA-87-0100, paper presented at the 25th Aerospace Sciences Meeting, Reno, Nevada, January 12-15, 1987.
3. Bragg, M. B. and Khodadoust, A., "Experimental Measurements in a Large Separation Bubble Due to a Simulated Glaze Ice Accretion", AIAA-88-0116, paper presented at the 26th Aerospace Sciences Meeting, Reno, Nevada, January 11-14, 1988.
4. Potapczuk, M. G., "Navier-Stokes Computations for a NACA 0012 Airfoil with Leading Edge Ice", AIAA Paper No. 87-0101, presented at the 25th Aerospace Sciences Meeting, Reno, Nevada, Jan. 12-15, 1987.
5. Cebeci, T., "Effects of Environmentally Imposed Roughness on Airfoil Performance", NASA CR 179639, June 1987.
6. Sankar, L. N., Wu, J. C. and Kwon, O. J., "Development of Two- and Three-Dimensional Navier-Stokes Solvers for Aircraft Icing Studies", presented at the Annual Airfoil Performance-icing Workshop, NASA Lewis Research Center, Cleveland, Ohio, July 25, 1988.
7. Bragg, M. B. and Khodadoust, A., "Effect of Simulated Glaze Ice On a Rectangular Wing", AIAA-89-0750, paper presented at the 27th Aerospace Sciences Meeting, Reno, Nevada, January 9-12, 1989.
8. Khodadoust, A. and Bragg, M. B., "Measured Aerodynamic Performance of a Swept Wing With a Simulated Glaze Ice Accretion", AIAA Paper 90-0490, 1990.
9. Bragg, M., Khodadoust, A., Soltani, R., Wells, S. and Kerho, M., "Effect of Simulated Ice Accretion on the Aerodynamics of a Swept Wing", AIAA-91-0442, paper presented at the 29th Aerospace Sciences Meeting, Reno, Nevada, Jan. 7-10, 1991.
10. Kwon, O. and Sankar, L., "Numerical Study of the Effects of Icing on Finite Wing Aerodynamics", AIAA-90-0757, paper presented at the 28th Aerospace Sciences Meeting, Reno, Nevada, January 8-11, 1990.
11. Sankar, L. and Kwon, L., "Numerical Studies of the Effects of Icing on Fixed and Rotary Wing Aircraft Aerodynamics", presentation at the Airfoil-icing Workshop, Nasa Lewis Research Center, Sept. 1990.
12. Rae, W. H. and Pope A., **Low-Speed Wind Tunnel Testing**, Second Edition, John Wiley & Sons, New York, 1984.
13. Bragg, M. B., Khodadoust, A. and Spring, S. A., "Experimental Measurements in a Large Leading-Edge Separation Bubble Due to a Simulated Airfoil Ice Accretion", to be published, **AIAA Journal**.

14. Tani, I., "Low Speed Flows Involving Bubble Separations", **Progress in Aeronautical Sciences**, Pergamon Press, 1964, pp. 70-103.

15. Briley, W. R. and McDonald, H., "Numerical Prediction of Incompressible Separation Bubbles", **Journal of Fluid Mechanics**, Vol. 69, June 1975, pp. 631-656.

16. Potapczuk, M.G., and Bragg, M.B., Kwon, O.J. and Sankar, L.N., "Simulation of Iced Wing Aerodynamics", 68th AGARD Fluid Dynamics Panel Specialists Meeting, Toulouse, France, April 29 - May 1, 1991.

17. Potapczuk, M. G., private communication, Dec. 1990.

**NACA 0012 ICING CONDITIONS**

$\alpha = 4^\circ$        $V = 130$  mph  
 $\bar{r} = 20\mu\text{m}$        $LWC = 2.1 \text{ g/m}^3$   
 $T = 18^\circ\text{F}$

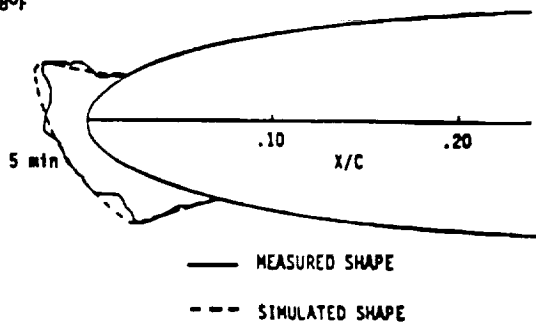


Fig. 1 Simulated Glaze Ice Accretion.

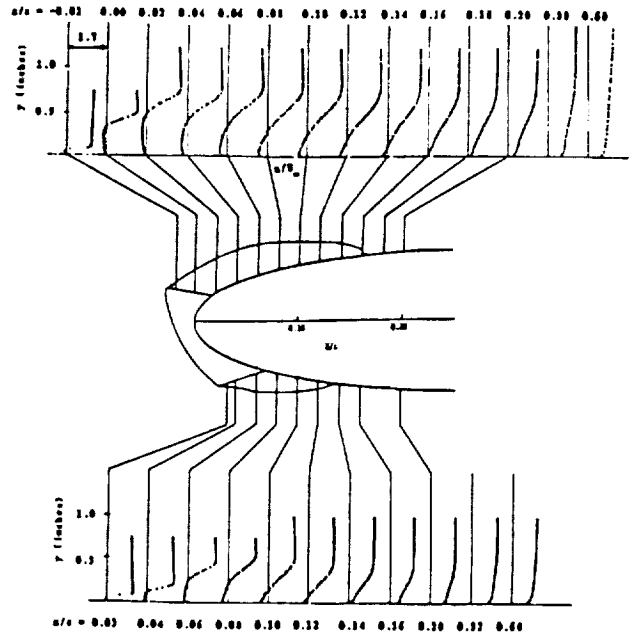


Fig. 3 Split Hot-Film Measurements on the NACA 0012 Airfoil with Simulated Ice at  $\alpha = 4$  deg.

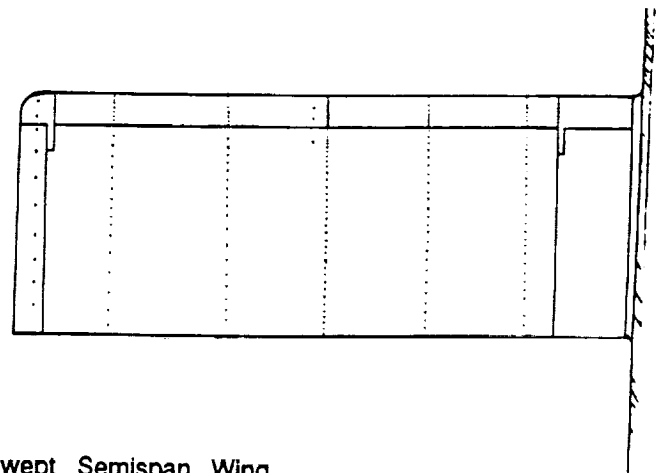
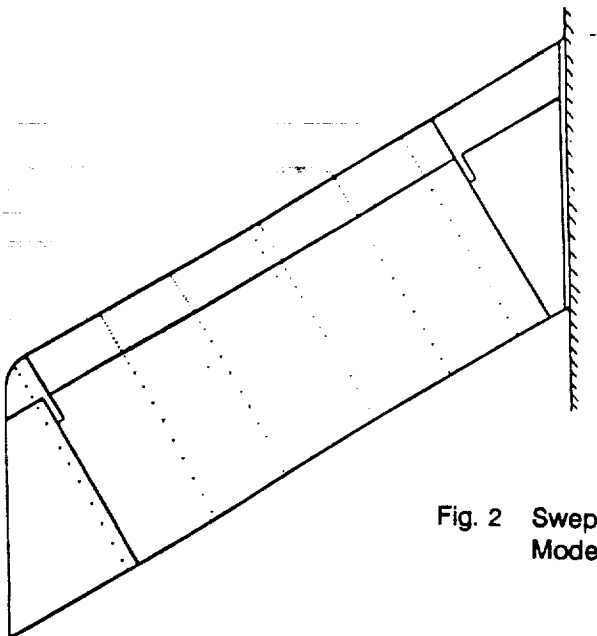


Fig. 2 Swept and Unswept Semispan Wing Models.

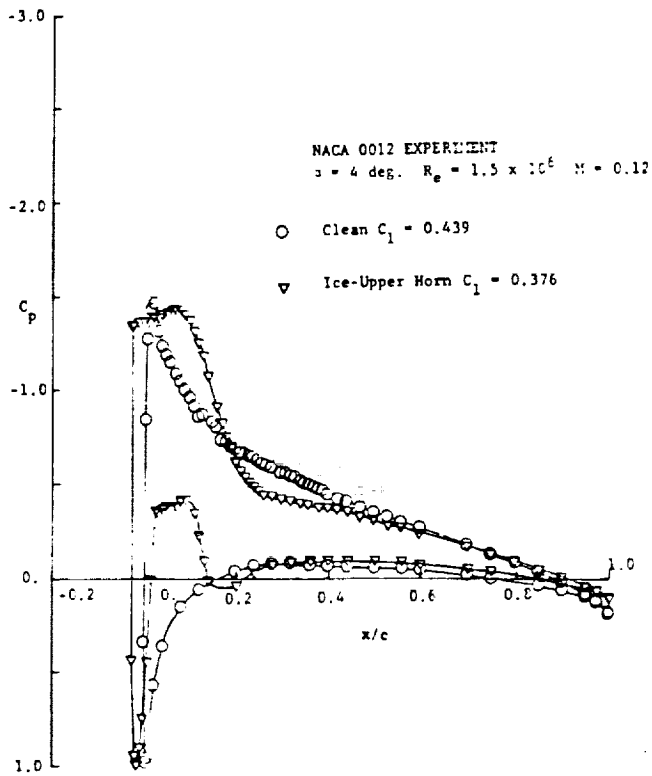


Fig. 4 Pressure Distribution on the NACA 0012 Airfoil With and Without Simulated Ice.

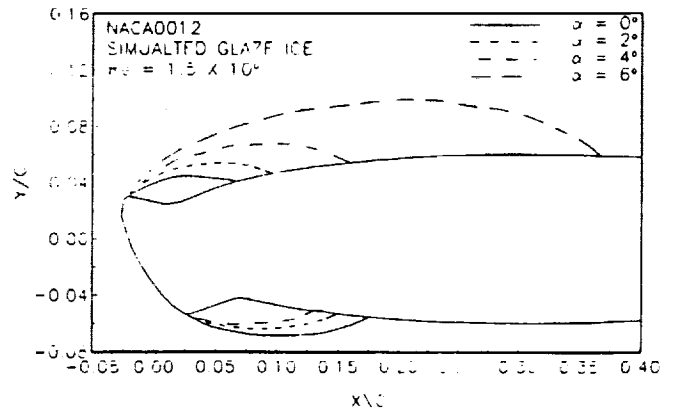


Fig. 5. Separation Streamlines on the NACA 0012 Airfoil With Simulated Glaze Ice.

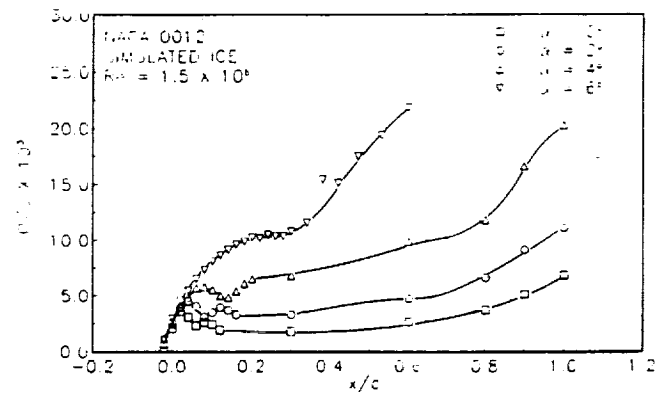


Fig. 6 Measured Momentum Thickness in the Upper Surface Separation Bubble.

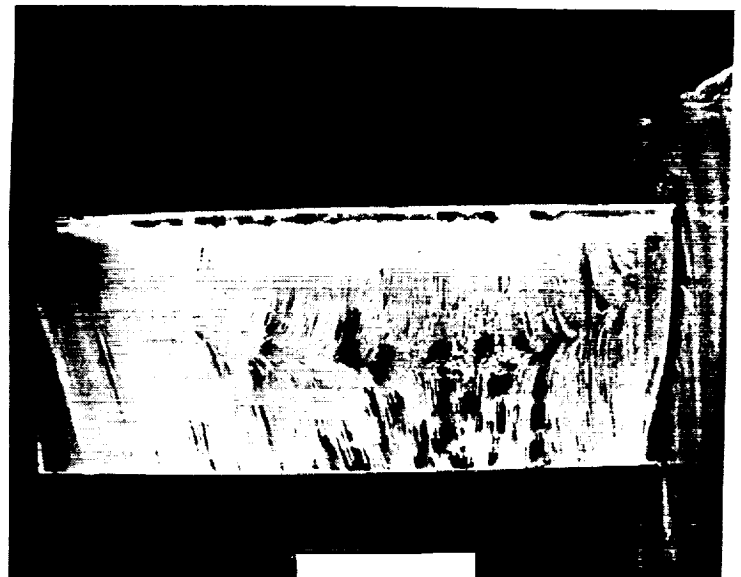
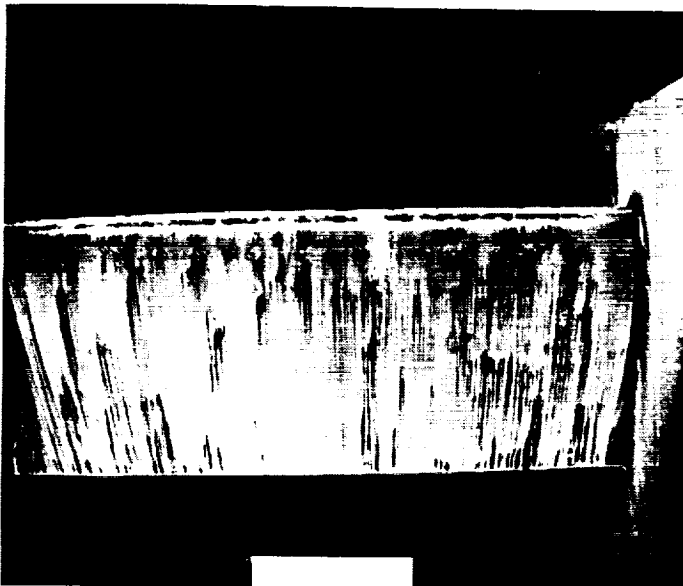


Fig. 7 Experimental Surface Oil Flow on the Straight Wing With Simulated Ice.

ORIGINAL PAGE IS OF POOR QUALITY

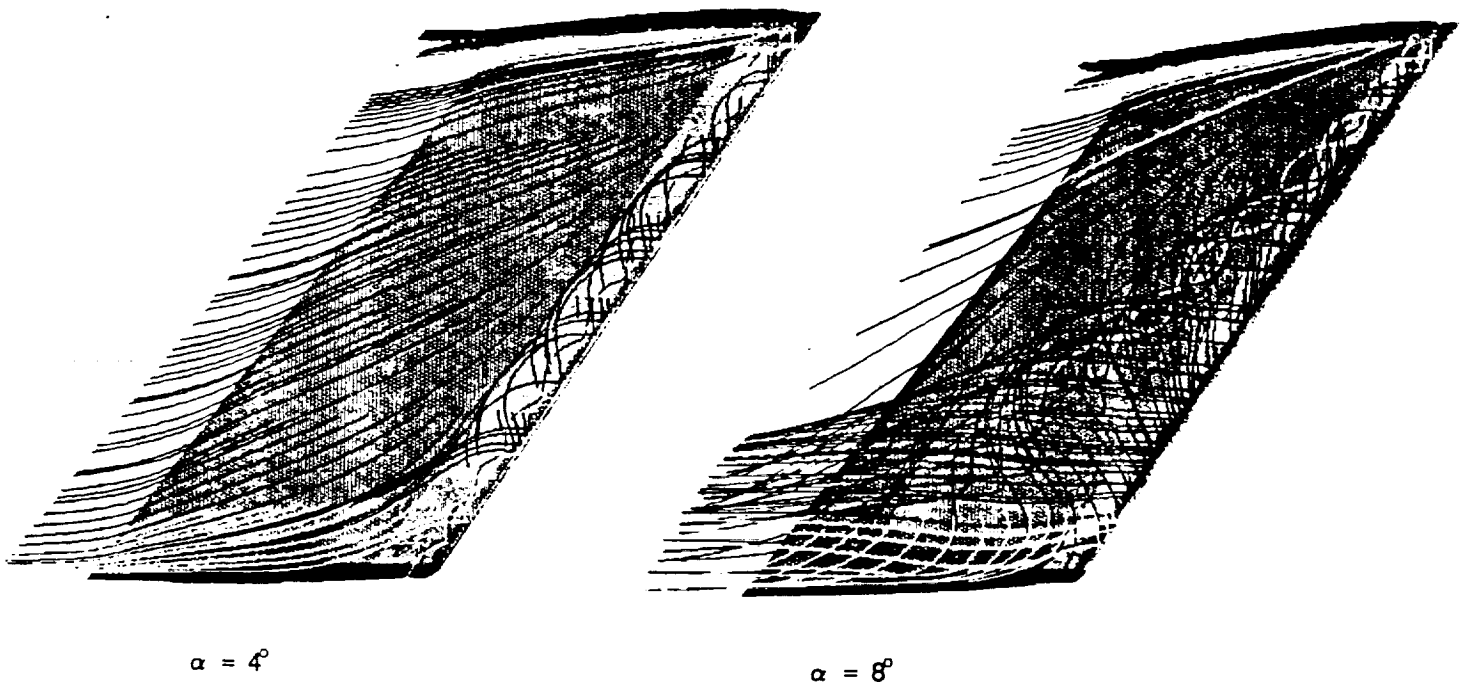


Fig. 8 Computational Flow Tracers on the Swept Wing With Simulated Ice<sup>17</sup>.

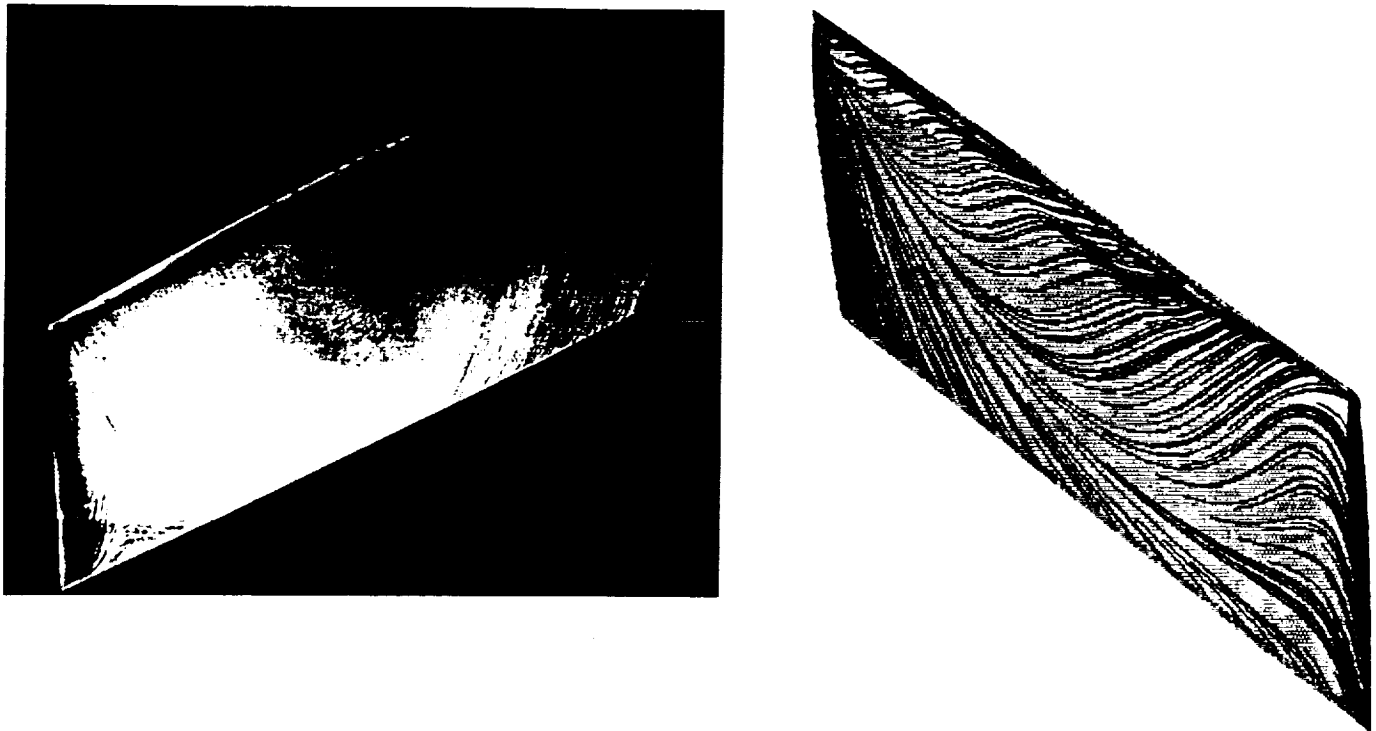


Fig. 9 Experimental and Computational<sup>17</sup> Surface Oil Flow on the Swept Wing With Ice at  $\alpha = 8$  deg.

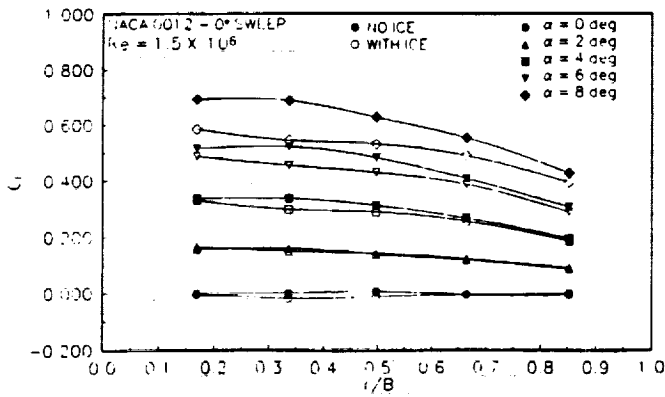


Fig. 10 Measured Span Loads for the Straight Wing With and Without Simulated Ice.

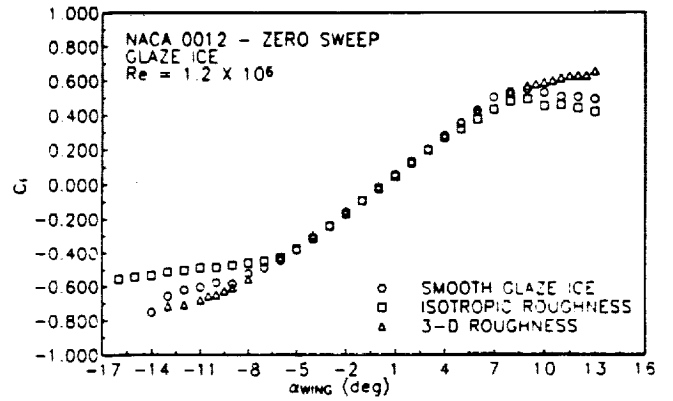


Fig. 12 Effect of Roughness Type on the Lift from the Centerline of the Unswept Wing With Ice.

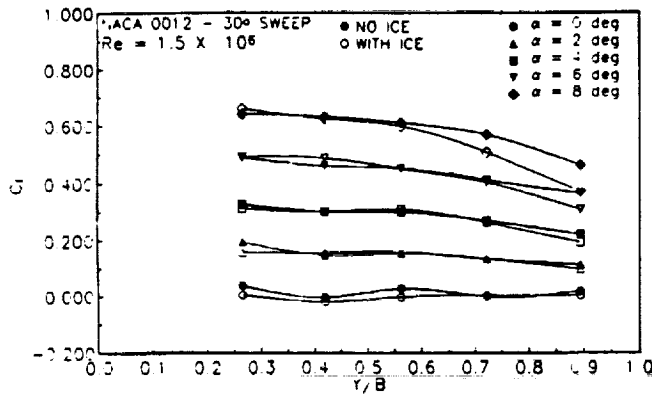


Fig. 11 Measured Span Loads for the Swept Wing With and Without Simulated Ice.

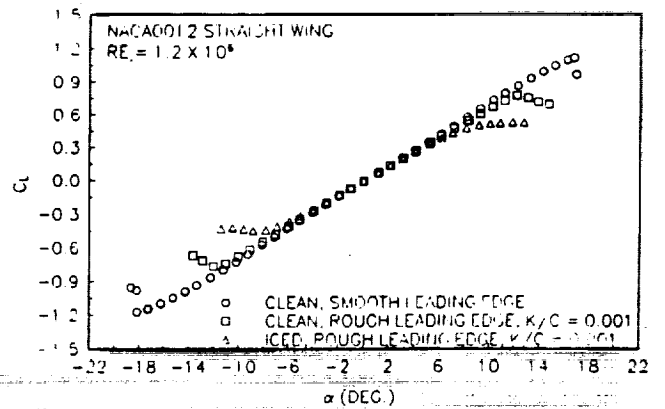


Fig. 13 Effect of Roughness on the Lift of the Unswept Wing With and Without Ice.